RSC Advances

PAPER

View Article Online
View Journal | View Issue



Cite this: *RSC Adv.*, 2019, **9**, 40835

# Lanthanide-doped mesoporous MCM-41 nanoparticles as a novel optical–magnetic multifunctional nanobioprobe†

Jun Liu,*[ab] Siqian Liu,[a] Yaling Li,[a] Jiayan Xue,[a] Youyi He,[a] Fuchi Liu,[a] Li Yang,[a] Junhui Hu,[a] Zhengye Xiong*[c] and Lizhen Long*[a]

Received 7th October 2019
Accepted 5th December 2019

DOI: 10.1039/c9ra08116j

rsc.li/rsc-advances

To research and develop potential multifunctional nanoprobes for biological application, lanthanide-doped MCM-41 (Ln-MCM-41, Ln = Gd/Eu) silica nanoparticles with excellent pore structure and optical–magnetic properties were synthesized *via* a facile and economical sol–gel method. The microstructure and pore distribution of Ln-MCM-41 nanoparticles were obviously affected by the Ln-doping. As the Ln/Si mole ratio increased, the specific surface area and total pore volume of Ln-MCM-41 nanoparticles rapidly decreased. However, the Ln-MCM-41 nanoparticles still retained the typical well-ordered mesoporous structure, and exhibited excellent drug release behavior. Moreover, the drug release rate of Ln-MCM-41 was remarkably pH-dependent and increased gradually upon decreasing pH. Additionally, these nanoparticles also exhibit considerable photoluminescence properties, living cells photoluminescence imaging *in vitro*, and paramagnetism behavior at room temperature due to the $Ln^{3+}$-ions doping. Our research shows the possibility of our Ln-MCM-41 nanoparticles as multifunctional nanoprobes for application in bioseparation, bioimaging, and drug delivery.



## 1. Introduction

With fascinating optical properties like a large Stokes shift, long excited-state lifetimes, photo-chemical stability, and narrow emission bands, trivalent lanthanide ion ($Ln^{3+}$) doped nanoparticles have attracted significant attention in biological imaging,[1–4] biomolecule detection,[5–7] security encoding,[8–10] and cancer therapeutics.[11–13] Many efforts have been made to improve the luminescence performance by optimizing the size, shape, and doping concentration of the $Ln^{3+}$-doped luminescence nanoparticles. Among the investigated materials, $Ln^{3+}$-doped $NaYF_4$ nanoparticles are of particular interest due to their lowest phonon cutoff energy and highly controllable synthesis process.[14–16] In recent years, the partial or complete substitution of $Y^{3+}$ by $Gd^{3+}$ in $NaYF_4$ was demonstrated, and $Gd^{3+}$ in the resulted $NaGdF_4$ matrix can mediate energy migration from $Tm^{3+}$ to other emitting centers (*e.g.*, $Tb^{3+}$, $Eu^{3+}$, $Sm^{3+}$, and $Dy^{3+}$) to achieve enriched luminescence.[17,18] Meanwhile, the Gd also exhibits magnetic properties to fabricate optically and magnetically active bifunctional materials.[19,20] However, the preparation of the $Ln^{3+}$-doped $NaYF_4$ nanoparticles is not satisfactory, owing to their complex process, low production and source reagent limitation. Compared to fluorides, the oxide counterparts (*e.g.*, $Y_2O_3$, $Gd_2O_3$, and $ZrO_2$) also has been widely used as luminescence-magnetic host due its high chemical stability, low bio-toxicity, and more stable in aqueous circumstances.[21–23] Unfortunately, the development of mass-scale synthesis methods for homogeneous, ultrafine, and robust $Ln^{3+}$-doped oxide nanoparticles is one of the key materials challenges for commercialization and advanced applications.[24,25]

In addition, much effort has been expended to develop the biocompatible and multifunctional $Ln^{3+}$-doped luminescent nanoparticles in recent years, in order to meet the clinical needs. Silica coating is particularly promising for this purpose because these particles reveal a low cytotoxicity, they are readily available in various thicknesses, and their surface can be functionalized almost at will through facile surface modification. Therefore, silica-coated $Ln^{3+}$-doped nanoparticles have successfully used in biomedical applications, such as biomarkers, biosensors, and in anti-cancer therapy.[26–28] Moreover, the silica coating may be also useful as drug delivery vehicle, *e.g.* for mesoporous-silica (m-$SiO_2$), active biological compounds, like anticancer drug or photosensitizers can be adsorbed, due to its unique porous ordered structure.[29–31] What is more, the readily chemically modifiable surface enable the use of such materials in controlled drug delivery.[32] However, the preparation of these core–shell materials is generally related to

[a]College of Physics Science and Technology & Guangxi Key Laboratory of Nuclear Physics and Technology, Guangxi Normal University, Guilin 541004, P. R. China. E-mail: liujun719@163.com; longlzh@foxmail.com; Fax: +86-773-5846479; Tel: +86-773-5846479

[b]State Key Laboratory for Chemistry and Molecular Engineering of Medicinal Resources, Guilin 541004, P. R. China

[c]School of Electronics and Information Engineering, Guangdong Ocean University, Zhanjiang 524088, China. E-mail: xiongzhengye@139.com

† Electronic supplementary information (ESI) available. See DOI: 10.1039/c9ra08116j

a multistep process, including the synthesis of uniform luminescence nanoparticles, coating of silica, and tedious wash process, which is not only complicated, but also poor reproducibility.

In recent years, tremendous efforts have been devoted to synthesis the $Ln^{3+}$-doped silica materials, *e.g.*, silica nanoparticles,[33–35] silica nanorods,[36] silica film.[37] In addition to the excellent luminescence properties, the $Ln^{3+}$-doped silica materials possess many advantages, such as high uniformity, easy surface modification and easy control of reaction conditions. Despite the substantial merits, the application of $Ln^{3+}$-doped silica materials as nanoprobes in biomedical application is still insufficient. Inspired by these researches, we dedicated to synthesis the porous structured luminescence silica nanoparticles for multifunctional bioapplication in this work. With ordered cylindrical channels, the mesoporous MCM-41 silica nanoparticles can be used as the nanocontainer for excellent drug storage and sustained drug release properties.[31,38] Therefore, the MCM-41 nanoparticles were selected as host, and $Ln^{3+}$ ions as activators to synthesis $Ln^{3+}$-doped MCM-41 (Ln-MCM-41) nanoparticles *via* the sample CTAB assisted sol–gel method. The pore distribution and luminescence properties can be easily tailored by the adjusting of $Ln^{3+}$-doping concentration and selection of activators. This system seems to be ideal for bioseparation, targeting and tracking drug delivery based on its pore-structure, magnetic and luminescent properties.

## 2. Experimental

### 2.1 Materials and preparation of samples

$Gd_2O_3$ (99.99%), $Eu_2O_3$ (99.99%), tetraethylorthosilicate (TEOS, 99.99%), cetyltrimethylammonium bromide ($C_{16}$TAB), and doxorubicin (DOX, 98%) were purchased from Aladdin Reagent Co., Ltd. (China). Polyethylene glycol-4000 (PEG-4000) and ammonia ($NH_3 \cdot H_2O$, 25%) was purchased from Xilong Scientific (China). Deionized (DI) water was produced using Direct-Q3 water purification system.

The $Ln_2O_3$ (Ln = Gd/Eu) powders with definite ratio Gd : Eu = 95 : 5 were firstly dissolved in $HNO_3$ while heating with the water-bath method and stirring till excess nitric acid evaporated, and a certain amount of deionized water was subsequently added with stirring for 10 min to form 2.4 M $Ln(NO_3)_3$ solution. The Ln-MCM-41 nanoparticles was synthesized by the one-pot sol–gel method. The typical synthesis process is described as follows: 0.2 g of $C_{16}$TAB and 0.505 g PEG-4000 was dissolved in 100 mL of deionized water. 2 mL of 25% $NH_3 \cdot H_2O$ was then added to the vigorously stirred solution at room temperature, followed by the addition of 1 mL TEOS and a certain amount of $Ln(NO_3)_3$ solution. After one hour of stirring, the fine particle precipitate was centrifuged and dried in a freezer dryer. Finally, the samples were calcined at 500 °C for 5 h to remove the templates.

### 2.2 Characterization

The X-ray diffraction (XRD) patterns were obtained on the X-ray diffractometer (Bruker D8 Advance, Germany) instrument operated using the Cu Kα radiation. Transmission electron microscopy (TEM) images and energy dispersive X-ray spectroscopy (EDS) analysis were acquired using a JEM-3200FS microscopy (JEOL, Japan). The nitrogen adsorption/desorption measurements were performed on a specific surface and pore size analysis instrument (3H-2000PS, Beishide Instrument Technology (Beijing) Co., Ltd., China) at 77 K, and all samples were degassed at 200 °C for 3 h prior to the measurement. Fourier transform infrared spectroscopy (FTIR) spectra were collected in Agilent Cary 630 FTIR spectrometer in the range of 500 to 4000 $cm^{-1}$. The photoluminescence (PL) spectra were measured at ambient conditions by a fluorescence spectrofluorophotometer (Shimadzu RF-5301PC, Japan) using a Xe lamp as the light source. Magnetic hysteresis curve were measured at room temperature using vibrating sample magnetometer (VSM, LakeShore 7404, American).

### 2.3 Optical imaging of live cells

Raw264.7 cell lines were inoculated on a 96-well culture plate and then cultured in Dulbecco's modified Eagle's medium

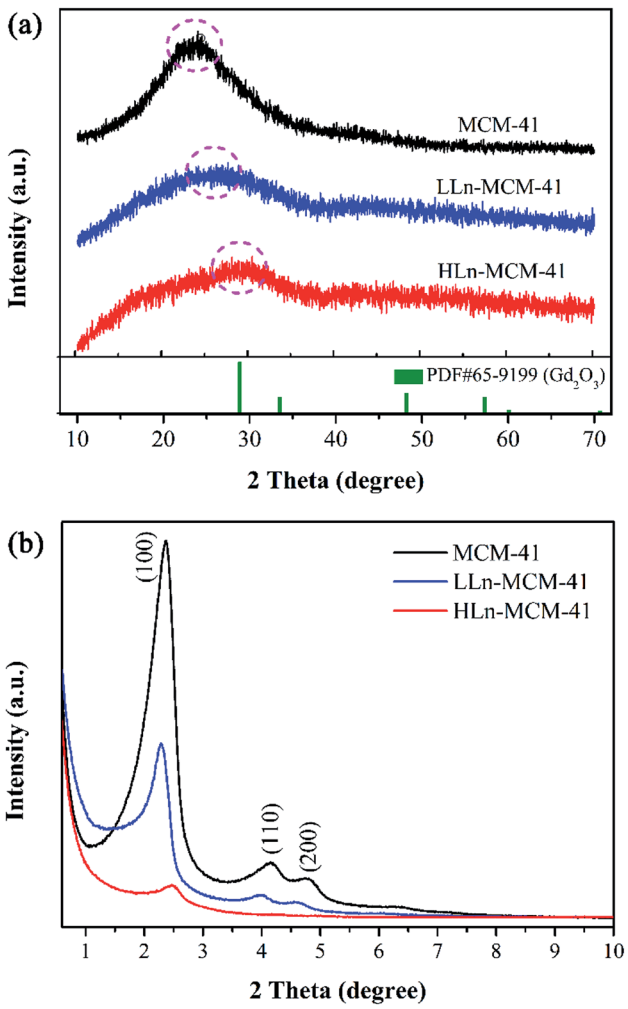


Fig. 1 (a) Wide-angle XRD and (b) small-angle XRD patterns of the mesoporous MCM-41, LLn-MCM-41, and HLn-MCM-41 nanoparticles.

(DMEM) supplemented with 10% fetal bovine serum, penicillin (100 units per mL) and streptomycin (100 mg $mL^{-1}$) at 37 °C under 5% $CO_2$ atmosphere. After growing to logarithmic growth phase, the cells were rinsed with phosphate buffered saline (PBS) and then were incubated with 50 μg $mL^{-1}$ of the Ln-MCM-41 in the same environment for another 2 h. After incubation, the cells were washed with PBS to remove the remaining particles and dead cells and then observed under a confocal fluorescence microscope (Leica TCS SP8, Germany).

### 2.4 Preparation of drug storage and delivery system

For the loading of DOX on the Ln-MCM-41 nanoparticles, 480 mg of the Ln-MCM-41 nanoparticles were dispersed in 80 mL phosphate buffer solution (PBS, pH = 7.4) with 40 mg DOX. After stirring for 2 h at room temperature, 3 mL of PA solution (5.0 mg $mL^{-1}$) was added and stirred for another 30 min. Subsequently, the pH value of the mixture was adjusted to alkaline. After then, 0.5 mL of 0.24 M $(NH_4)_3PO_4 \cdot 3H_2O$ solution and 0.5 mL of 0.29 M $Ca(NO_3)_2 \cdot 4H_2O$ solution were injected 8 times in turn at 10 min intervals. The as-fabricated product was collected by centrifugation at 10 000 rpm for 8 minutes and then freeze-dried under vacuum for 12 h dried at 60 °C, and the solid was named as DOX-Ln-MCM-41. UV-vis was used to determine the concentration of the separated supernatant solution. To evaluate the DOX-release behavior, 30 mg DOX-Ln-MCM-41 samples were immersed in 10 mL PBS solution (pH = 7.4, 6.5, or 5.5) at 37 °C under continuous stirring. At predetermined time intervals, 3 mL of the released medium was taken and centrifuged. The amount of released DOX was measured by a UV-vis spectrophotometer (Shimadzu UV-2700, Japan) at a wavelength of 480 nm. Finally, the medium taken out for measurement was returned to the original released medium.

## 3. Results and discussion

To investigate the influence of $Ln^{3+}$-ions doping on the pore properties of the Ln-MCM-41 nanoparticles, three samples with zero, low (0.07), high (0.13) mole ratio of Ln/Si (Ln = Gd/Eu, Gd : Eu = 95 : 5) were synthesized and denotes as pristine MCM-41, LLn-MCM-41, and HLn-MCM-41, respectively (see the details in Table S1†). The wide-angle XRD pattern (Fig. 1a) of

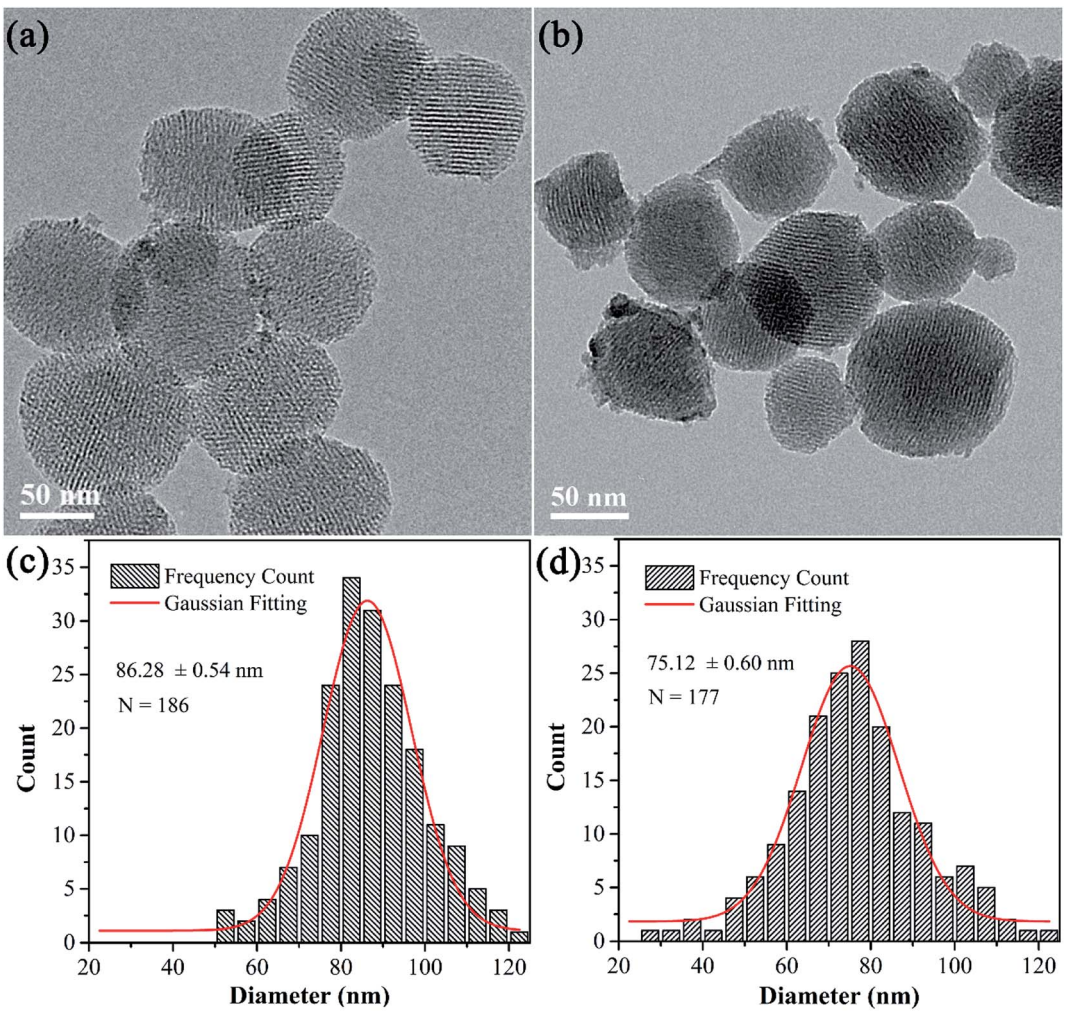


Fig. 2 Typical TEM image of MCM-41 (a) and HLn-MCM-41 (b) nanoparticles, and their corresponding size distribution histogram (c and d).

pristine MCM-41 exhibit a broad diffraction peak at $2\theta$ values between 15.0° and 35.0°, which is typical for amorphous silica. By doping with $Ln^{3+}$-ions, the amorphous diffraction peak remarkably reduced for both the LLn-MCM-41 and HLn-MCM-41. Small-angle XRD patterns (Fig. 1b) recorded at the range of 0.5° to 10° show a very intense (100) Bragg diffraction and two less intense (110) and (200) diffraction peaks reflections associated with a *p*6 mm hexagonal symmetry of the ordered MCM-41-type materials.[38] Obviously, the incorporation of heteroatoms into the silica not only decreased the peak intensity but also caused the shift of $d_{100}$-spacing relative to undoped MCM-41. However, the shift of $d_{100}$-spacing for LLn-MCM-41 toward to the large value, while the $d_{100}$-spacing for HLn-MCM-41 shifted to a small value. The incorporation of heteroatoms into the silica pore framework or the formation of Gd and Eu oxide clusters may cause the shift in $d_{100}$-spacing.

The morphology of the Ln-MCM-41 nanoparticles were further observed by TEM measurements. As presented in Fig. 2a and b, the TEM image of the MCM-41 and HLn-MCM-41 nanoparticles revealed their well-defined ordered pore structure. The pore structure of MCM-41 nanoparticles is clearer than that of HLn-MCM-41. The mean diameters based on the corresponding size distribution histogram (Fig. 2c and d) were determined to ~86.28 for MCM-41 and ~75.12 nm for HLn-MCM-41, respectively. Additionally, the HLn-MCM-41 nanoparticles possess a broader size distribution compared to MCM-41. These results revealed that the $Ln^{3+}$-doping promotes the formation of small-sized particles.

In addition, we also noticed that some regions of the Ln-doped MCM-41 nanoparticles are darker than other regions or pristine MCM-41 nanoparticles, or some particles seem have coating layer on the surface, according to the TEM images in Fig. 2b. These zones may be rich in the incorporation of

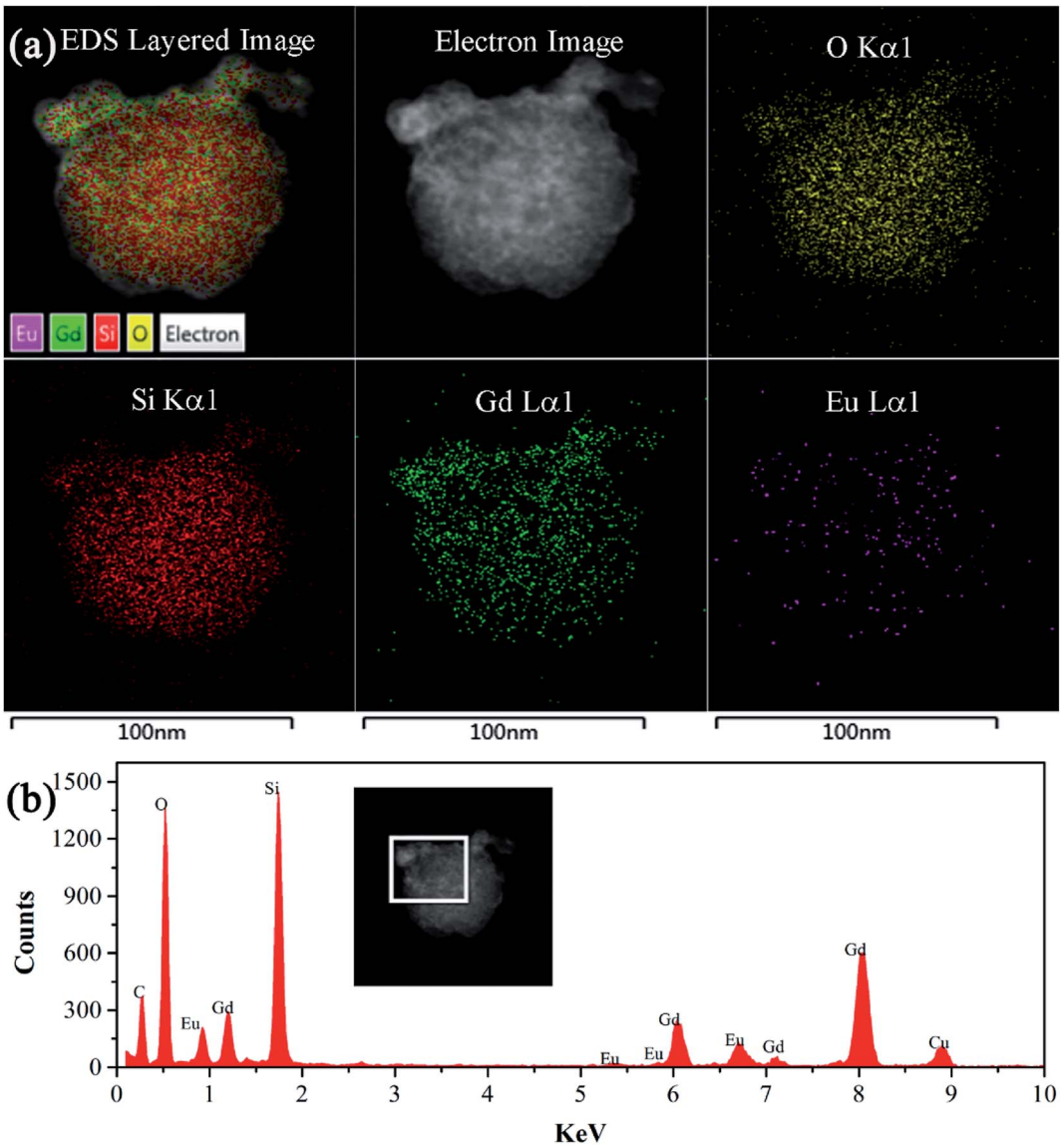


Fig. 3 (a) Elemental mapping and (b) EDS spectrum of the HLn-MCM-41 nanoparticles.

 

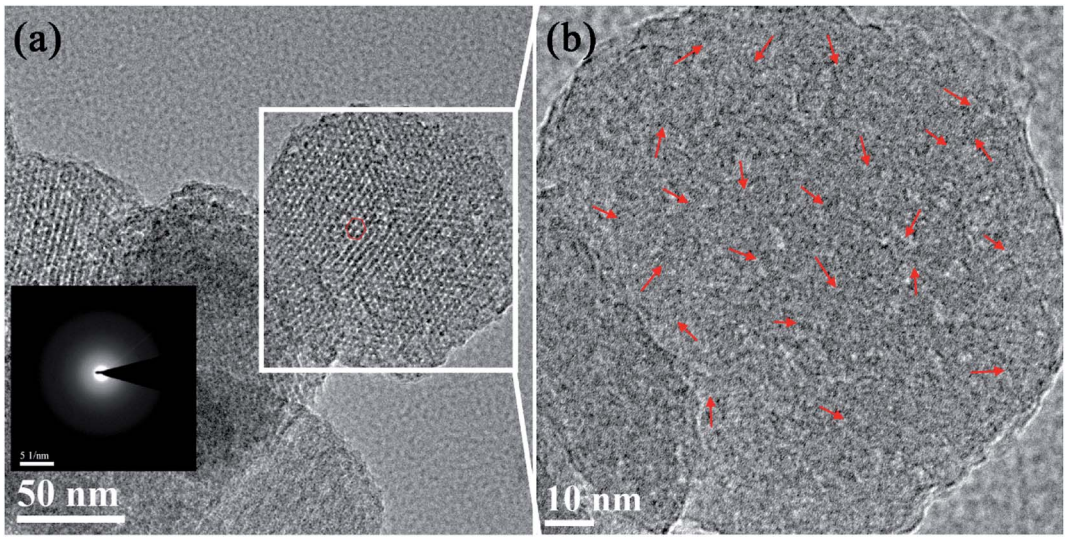


Fig. 4 (a) TEM image and SAED pattern taken with the electron beam parallel to the pore direction of the HLn-MCM-41 nanoparticles; (b) HR-TEM image of the HLn-MCM-41 nanoparticles.

heteroatoms Eu and Gd. Thus, the TEM-EDS mapping (Fig. 3a) were employed to check these nanoparticles. The elemental mappings clearly reveal that the elements of Gd and Eu are unevenly distributed, or there is aggregation in Gd and Eu. From the TEM-EDS (Fig. 3b) of HLn-MCM-41 nanoparticles, signals of O, Si, Gd, and Eu can be surveyed, demonstrating the successful doping of Gd and Eu into MCM-41. The carbon (C) and copper (Cu) peaks in EDS spectrum probably comes from the TEM-grid.

To confirm the reason of the aggregation in Gd and Eu, the SAED pattern and high-resolution TEM (HR-TEM) analysis of the HLn-MCM-41 nanoparticles was further studied. In the TEM image (Fig. 4a) taken with the electron beam parallel to the pore direction of the HLn-MCM-41 nanoparticles, the pores present an ordered hexagonal structure. The SAED pattern (the insert in Fig. 4a) of the HLn-MCM-41 nanoparticles is consistent with the amorphous structure diffraction pattern, which is in accordance with the wide-angel XRD results. However, some tiny lattice streaks can be observed in HR-TEM image (Fig. 4b). These tiny lattice fringes indicate the presence of fine crystalline grains in the HLn-MCM-41 nanoparticles, and these grains may be the Gd or Eu oxide clusters.

Fig. 5 shows the nitrogen adsorption/desorption isotherms and pore-size distribution curves of all samples. The isotherm of MCM-41 exhibit a typical type IV behavior with an H1-type hysteresis loop (Fig. 5a), which is typical for mesoporous materials with two-dimensional hexagonal structures.[39] The $N_2$ uptake at low relative pressure ($P/P_0$ < 0.1) for all samples indicates the existence of micropores. No obvious hysteresis loop is observed above a relative pressure of 0.9, but a sharp step increase at $P/P_0 = 0.25$–$0.35$ in the isotherm of the MCM-41 both the well-ordered mesoporous structure and the uniformity of the pore size distribution of the sample. The decrease of the absorption amount of LLn-MCM-41 and HLn-MCM-41 can be attributed to the reduced surface area, whereas the shift of inflection point of the step to lower relative pressure $P/P_0$ is caused by the smaller mesopores size, which can be associated with the pore-filling effect. The pore-size distribution curves (Fig. 5b), derived from the desorption branch based on the

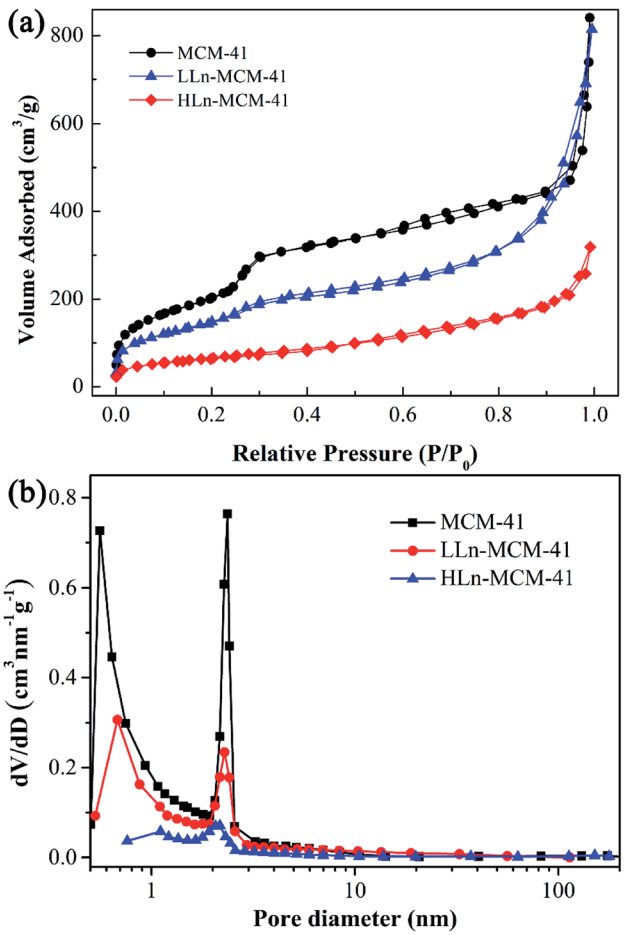


Fig. 5 Porous textures of the samples. (a) Nitrogen adsorption–desorption isotherms, and (b) pore size distribution curves calculated from the desorption branch of the isotherm.

Table 1 The calculated structural parameters of all samples

| Samples | $S_{BET}$ ($m^2$ $g^{-1}$) | Total pore volume (mL $g^{-1}$) | Micropore volume (mL $g^{-1}$) | | | Proportion of micropore |
|---|---|---|---|---|---|---|
| | | | *T*-plot | H–K | DR | |
| MCM-41 | 910 | 1.30 | 0.31 | 0.27 | 0.30 | <24% |
| 0.07 Gd/Eu-MCM-41 | 612 | 1.26 | 0.16 | 0.20 | 0.21 | <17% |
| 0.13 Gd/Eu-MCM-41 | 281 | 0.77 | 0.06 | 0.07 | 0.08 | <10% |

density functional theory (DFT), reveals the presence of relatively uniform micropores and mesopores in all samples. The calculated structural parameters of all samples are listed in Table 1. The specific surface area ($S_{BET}$) was calculated using the Brunauer–Emmett–Teller (BET) based on adsorption data in the partial pressure ($P/P_0$) range of 0.04–0.32. The specific surface area rapidly drops from 910 $m^2$ $g^{-1}$ of MCM-41 to 281 $m^2$ $g^{-1}$ of HLn-MCM-41, while the total pore volume decreases from 1.30 mL $g^{-1}$ to 0.77 mL $g^{-1}$, respectively. Mesopores are the major pores in Ln-MCM-41 nanoparticles, while micropores are minor with a decreased proportion by increasing of $Ln^{3+}$ doping amount.

Lanthanide-based nanoparticles have excellent and diverse photoluminescence properties, thus we further studied the

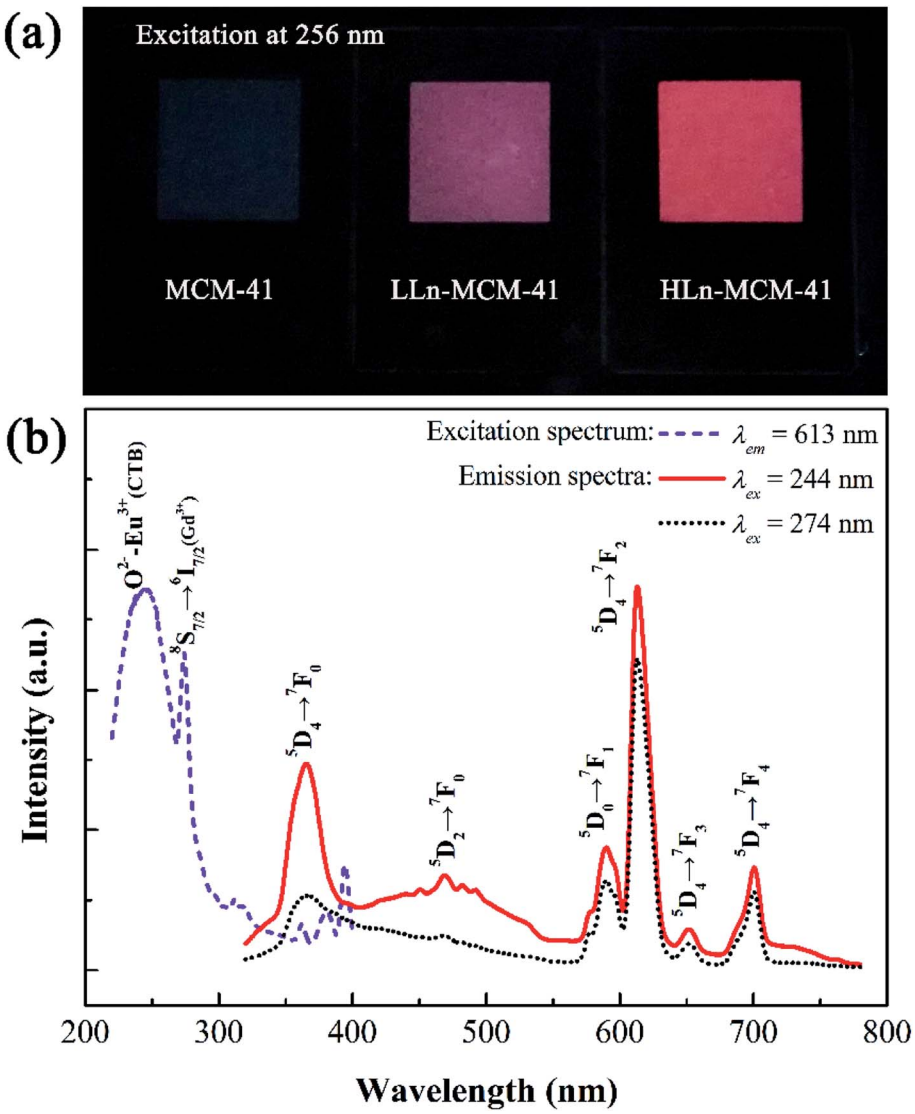


Fig. 6 (a) Photoluminescence photograph of MCM-41, LLn-MCM-41, and HLn-MCM-41 nanoparticles under excitation at 256 nm; (b) room temperature photoluminescence excitation (PLE) and photoluminescence emission (PL) properties of the HLn-MCM-41 nanoparticles.

 

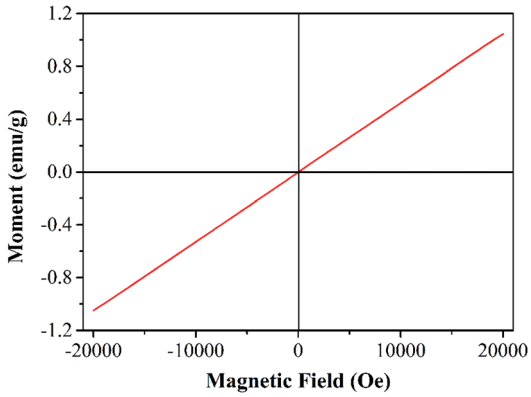


Fig. 7 RT magnetization as a linear function of magnetic field for the HLn-MCM-41 nanoparticles.

photoluminescence properties of the Ln-MCM-41 nanoparticles. Fig. 6a gives the luminescence photograph of the MCM-41, LLn-MCM-41, and HLn-MCM-41 powders, which was recorded by a digital camera without using any optical filters under excitation with ultraviolet light (365 nm). Red emission can be clearly observed from Ln-MCM-41 nanoparticles at room temperature, and no emission for undoped MCM-41. Obviously, the luminescence intensity of Ln-MCM-41 nanoparticles increased with the increase of $Ln^{3+}$ doping amount. Fig. 6b demonstrates the room temperature photoluminescence excitation (PLE) and photoluminescence emission (PL) spectra of HLn-MCM-41 nanoparticles. The PLE spectrum monitored by 613 nm ($^5D_4 \rightarrow {}^7F_2$ energy levels transition of $Eu^{3+}$ ions) exhibit a strong broad excitation peak centering at 244 nm corresponding to the $O^{2+}$–$Eu^{3+}$ charge transfer band (CTB) adsorption, and a weak sharp excitation peak at 274 nm may assigned to $Gd^{3+}$ ($^8S_{7/2} \rightarrow {}^6I_{7/2}$), suggesting the energy transfer occurred from the $Gd^{3+}$ ions to the $Eu^{3+}$ ions.[40] Upon excitation at 244 and 274 nm, the $Gd^{3+}/Eu^{3+}$ co-doped MCM-41 nanoparticles exhibit characteristic emission spectrum. The emission peaks originate from $^5D_i \rightarrow {}^7F_J$ energy levels transitions of $Eu^{3+}$, *i.e.*, $^5D_4 \rightarrow {}^7F_0$ (362 nm), $^5D_2 \rightarrow {}^7F_0$ (464 nm), $^5D_0 \rightarrow {}^7F_1$ (594 nm), $^5D_0 \rightarrow {}^7F_2$ (613 nm), $^5D_0 \rightarrow {}^7F_3$ (653 nm), and $^5D_0 \rightarrow {}^7F_4$ (701 nm).[41] To obtain multicolored Ln-MCM-41 fluorescence nanoparticles, the different ion-combinations including $Gd^{3+}/Tm^{3+}$ and $Gd^{3+}/Tb^{3+}$, were also introduced to synthesis the blue and green Ln-MCM-41 luminescence nanoparticles (Fig. S1†).

In addition to the excellent fluorescent properties, lanthanide-based nanoparticles also possess commendable magnetic properties and thus could be used as important materials for magnetic resonance imaging (MRI) and bioseparation. Magnetization as a function of magnetic fields of the HLn-MCM-41 nanoparticles is shown in Fig. 7. Keeping the total doping concentration and Gd content as the constants, the magnetization curves obtained by using Gd/Eu, Gd/Tb and Gd/Tm co-doped nanoparticles are very similar (as shown in Fig. S2†). The HLn-MCM-41 nanoparticles show paramagnetism at RT, unlike the magnetic response behavior of Gd atoms which exhibit ferromagnetism below 289 K. In general, the magnetic properties of $Gd^{3+}$ arise from seven unpaired inner 4f electrons which are closely bound to the nucleus and effectively shielded by the outer closed shell electrons $5s^2$ $5p^6$. According to the M–H relationship, the magnetic mass susceptibilities of HLn-MCM-41 nanoparticles are $5.26 \times 10^{-5}$ emu $g^{-1}$ $Oe^{-1}$, respectively. The magnetization of HLn-MCM-41 nanoparticles at 20 kOe is about 1.04 emu $g^{-1}$, which is close to the reported magnetite in bioseparation and bioimaging (as shown in Table S2†).

To verify the feasibility of using Ln-MCM-41 nanoparticles as bioimaging probes, the Raw264.7 living cells incubated with the HLn-MCM-41 nanoparticles were imaged under the laser confocal fluorescence microscope. The preprocessed cells were imaged by laser scanning microscope excited at 488 nm. As shown in Fig. 8, the HLn-MCM-41 nanoparticles maintain intrinsically significant photoluminescence characteristics after being swallowed by the cells. The overlay images reveal that the red fluorescence are unevenly and mainly distributed in the cytoplasm, which is regarded to the heterogeneous distribution of the sample inside the cell. The result validate that the HLn-MCM-41 nanoparticles, verified to possess both good cell compatibility and cell internalization, are qualified for the function of live cell imaging.

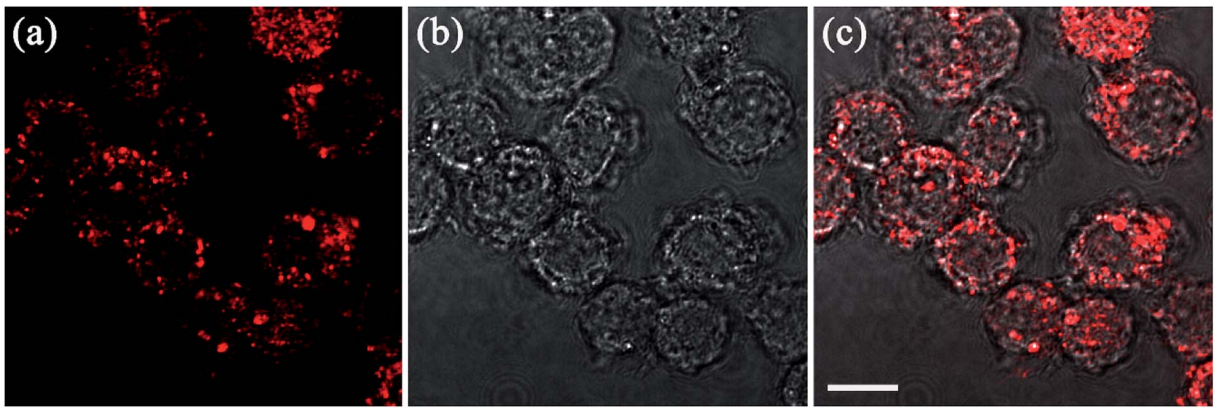


Fig. 8 Confocal laser microscope images of Raw 264.7 cells incubated with HLn-MCM-41 nanoparticles: (a) fluorescence, (b) bright-field, and (c) overlay images (scale bar: 10 μm).

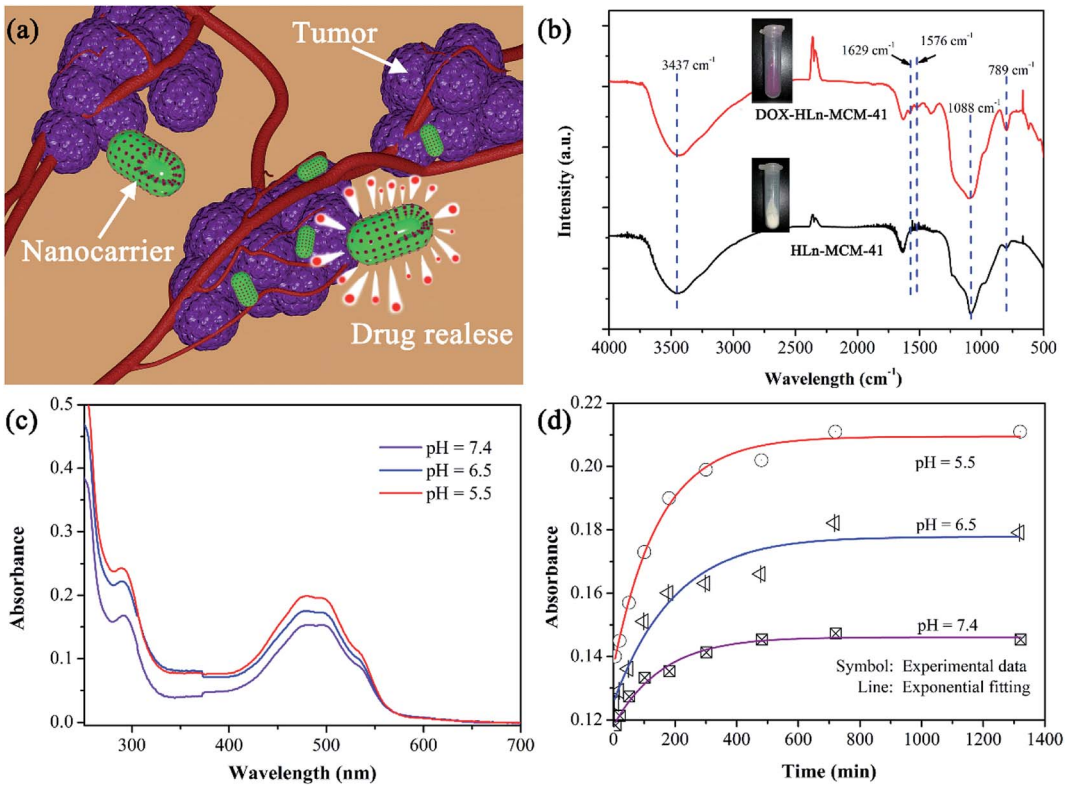


Fig. 9 (a) Schematic illustrations of DOX release behavior for HLn-MCM-41 nanoparticles; (b) FTIR spectra of HLn-MCM-41 and DOX-HLn-MCM-41 samples; (c) UV-vis absorbance spectra of the PBS medium after 5 h release at three different pH values; (d) real time monitoring absorbance in 480 nm of the released medium at three different pH values and the corresponding exponential curve fitting.

The mesoporous nanoparticles can be used as the nanocontainer for excellent drug storage and sustained drug release properties. Although the pore properties of the Ln-MCM-41 nanoparticles are affects by the $Ln^{3+}$-doping, we found that they still possess commendable properties of nanocarriers. As shown in Fig. 9a, we selected the HLn-MCM-41 nanoparticles as nanocarriers and doxorubicin (DOX) as a model drug to evaluate the drug storage and release behavior in our experiment. It can be calculated that the loading mount of DOX-Ln-MCM-41 nanoparticles were ~0.06 mg of the DOX per mg of nanoparticles, based on the UV-vis absorbance analysis of the PBS medium measured at different loading time (as shown in Fig. S3†). FT-IR (Fig. 9b) was used to investigate the drug loading. A broad band in the region of 3437 $cm^{-1}$ was attributed to the symmetric stretching of OH groups from Si–OH in HLn-MCM-41 and DOX-HLn-MCM-41. They also show the main peaks characteristic of silica in the region around 1088 and 789 $cm^{-1}$ corresponding to symmetrical and a symmetrical stretching vibration of Si–O–Si. Two characteristic absorption peaks at 1629 and 1576 $cm^{-1}$ are ascribed to the C=O stretching vibration from the anthraquinone ring of DOX in DOX-HLn-MCM-41 sample. The supernatant solution was determined to obtain the residual DOX content by UV-vis measurement. As seen in Fig. 9c, the DOX release amount could be determined by the characteristic DOX absorbance intensity peaked at 480 nm. The *in vitro* real time monitoring release profiles and absorption spectra of DOX from DOX-HLn-MCM-41 nanoparticles in PBS buffer solution at different pH value are shown in Fig. 9d and S4.† The drug release rate of DOX-HLn-MCM-41 was remarkably pH-dependent and increased gradually upon decreasing pH. The pH-sensitive DOX released from nanoparticles might be beneficial for controlled drug delivery and release into cancer cells since the microenvironments in intracellular lysosomes, endosomes and certain cancerous tissues is acidic.

## 4. Conclusion

In summary, the $Ln^{3+}$-doped MCM-41 (Ln-MCM-41) nanoparticles with excellent pore structure and optical–magnetic properties have been successfully prepared *via* a simple one-pot route. The prepared Ln-MCM-41 nanoparticles exhibit typical well-ordered mesoporous structure. As the Ln/Si mole ratio increased from 0 to 0.13, the specific surface area of Ln-MCM-41 nanoparticles drops from 910 to 281 $m^2\ g^{-1}$, and the total pore volume decrease from 1.30 to 0.77 mL $g^{-1}$. Further work demonstrated that although the pore volume is reduced, the capability of Ln-MCM-41 nanoparticles as a drug carrier is still satisfactory. Moreover, the drug release behavior of Ln-MCM-41 nanoparticles was pH-sensitive, and the drug release rate was increased gradually upon decreasing pH. The Ln-MCM-41 nanoparticles also exhibit excellent photoluminescence properties and considerable magnetic mass susceptibility. In fact,

 

this work is expected to develop an optical–magnetic MCM-41 nanoparticles, which promises potential applications in a wide range of fields such as bioseparation, optical–magnetic bioimaging, and drug delivery.

## Conflicts of interest

There are no conflicts to declare.

## Acknowledgements

This work was supported by the Natural Science Foundation of Guangxi (No. 2018GXNSFBA138007, 2018GXNSFBA281073, 2018GXNSFAA294021), the National Natural Science Foundation of China (No. 11665007, 11664003), the Guangxi Key Research and Development Program (No. AB18221033), the State Key Laboratory for Chemistry and Molecular Engineering of Medicinal Resources (Guangxi Normal University, No. CMEMR2018-B11), the PhD Start-up Fund of Guangxi Normal University (No. 2017BQ023, 2017BQ006), and the Innovation Project of Guangxi Graduate Education (No. XYCSZ2019058).

## Notes and references

1 T. Maldiney, A. Bessière, J. Seguin, E. Teston, S. K. Sharma, B. Viana, A. J. J. Bos, P. Dorenbos, M. Bessodes, D. Gourier, D. Scherman and C. Richard, *Nat. Mater.*, 2014, **13**, 418–426.
2 Q. Liu, W. Feng, T. Yang, T. Yi and F. Li, *Nat. Protoc.*, 2013, **8**, 2033.
3 D. H. Ortgies, M. Tan, E. C. Ximendes, B. del Rosal, J. Hu, L. Xu, X. Wang, E. Martín Rodríguez, C. Jacinto, N. Fernandez, G. Chen and D. Jaque, *ACS Nano*, 2018, **12**, 4362–4368.
4 A. Bednarkiewicz, E. M. Chan, A. Kotulska, L. Marciniak and K. Prorok, *Nanoscale Horiz.*, 2019, **4**, 881–889.
5 Z. Zhang, S. Shikha, J. Liu, J. Zhang, Q. Mei and Y. Zhang, *Anal. Chem.*, 2019, **91**, 548–568.
6 X. Lei, R. Li, D. Tu, X. Shang, Y. Liu, W. You, C. Sun, F. Zhang and X. Chen, *Chem. Sci.*, 2018, **9**, 4682–4688.
7 Z. Chen, W. Zheng, P. Huang, D. Tu, S. Zhou, M. Huang and X. Chen, *Nanoscale*, 2015, **7**, 4274–4290.
8 Y. Lu, J. Zhao, R. Zhang, Y. Liu, D. Liu, E. M. Goldys, X. Yang, P. Xi, A. Sunna and J. Lu, *Nat. Photonics*, 2014, **8**, 32–36.
9 Y. Lu, J. Zhao, R. Zhang, Y. Liu, D. Liu, E. M. Goldys, X. Yang, P. Xi, A. Sunna, J. Lu, Y. Shi, R. C. Leif, Y. Huo, J. Shen, J. A. Piper, J. P. Robinson and D. Jin, *Nat. Photonics*, 2013, **8**, 32.
10 X. Wen, T. K. Lee, B. E. Moon, H. Song, C. Xu, B. Chun, Y. I. Kim, K. K. Sang, C. Peng and D. Kim, *Adv. Opt. Mater.*, 2018, **6**, 1701119.
11 L. Cheng, K. Yang, Y. Li, X. Zeng, M. Shao, S.-T. Lee and Z. Liu, *Biomaterials*, 2012, **33**, 2215–2222.
12 N. M. Idris, M. K. Gnanasammandhan, J. Zhang, P. C. Ho, R. Mahendran and Y. Zhang, *Nat. Med.*, 2012, **18**, 1580–1585.
13 J. Zuo, L. Tu, Q. Li, Y. Feng, I. Que, Y. Zhang, X. Liu, B. Xue, L. J. Cruz, Y. Chang, H. Zhang and X. Kong, *ACS Nano*, 2018, **12**, 3217–3225.
14 F. Wang, Y. Han, C. S. Lim, Y. Lu, J. Wang, J. Xu, H. Chen, C. Zhang, M. Hong and X. Liu, *Nature*, 2010, **463**, 1061–1065.
15 R. Deng, F. Qin, R. Chen, W. Huang, M. Hong and X. Liu, *Nat. Nanotechnol.*, 2015, **10**, 237–242.
16 J. Zhao, D. Jin, E. P. Schartner, Y. Lu, Y. Liu, A. V. Zvyagin, L. Zhang, J. M. Dawes, P. Xi, J. A. Piper, E. M. Goldys and T. M. Monro, *Nat. Nanotechnol.*, 2013, **8**, 729–734.
17 S. Han, X. Qin, Z. An, Y. Zhu, L. Liang, Y. Han, W. Huang and X. Liu, *Nat. Commun.*, 2016, **7**, 13059.
18 C. Dong, A. Korinek, B. Blasiak, B. Tomanek and F. C. J. M. van Veggel, *Chem. Mater.*, 2012, **24**, 1297–1305.
19 X. Zhang, Z. Zhao, X. Zhang, D. B. Cordes, B. Weeks, B. Qiu, K. Madanan, D. Sardar and J. Chaudhuri, *Nano Res.*, 2015, **8**, 636–648.
20 G. Chen, T. Y. Ohulchanskyy, W. C. Law, H. Ågren and P. N. Prasad, *Nanoscale*, 2011, **3**, 2003–2008.
21 Z. Liu, F. Pu, S. Huang, Q. Yuan, J. Ren and X. Qu, *Biomaterials*, 2013, **34**, 1712–1721.
22 J. Liu, L. Huang, X. Tian, X. Chen, Y. Shao, F. Xie, D. Chen and L. Li, *Int. J. Nanomed.*, 2017, **12**, 1–14.
23 M. Wu, G. Guan, B. Yao, C.-P. Teng, S. Liu, S. Y. Tee, B. C. Ong, Z. Dong and M.-Y. Han, *ACS Appl. Nano Mater.*, 2019, **2**, 1421–1430.
24 J. Liu, X. Tian, N. Luo, C. Yang, J. Xiao, Y. Shao, X. Chen, G. Yang, D. Chen and L. Li, *Langmuir*, 2014, **30**, 13005–13013.
25 J. Leng, J. Chen, D. Wang, J.-X. Wang, Y. Pu and J.-F. Chen, *Ind. Eng. Chem. Res.*, 2017, **56**, 7977–7983.
26 M. Back, E. Trave, G. Zaccariello, D. Cristofori, P. Canton, A. Benedetti and P. Riello, *Nanoscale*, 2019, **11**, 675–687.
27 M. Runowski, N. Stopikowska, D. Szeremeta, S. Goderski, M. Skwierczyńska and S. Lis, *ACS Appl. Mater. Interfaces*, 2019, **11**, 13389–13396.
28 R. Tian, S. Zhao, G. Liu, H. Chen, L. Ma, H. You, C. Liu and Z. Wang, *Biomaterials*, 2019, **212**, 64–72.
29 J. Xu, P. Yang, M. Sun, H. Bi, B. Liu, D. Yang, S. Gai, F. He and J. Lin, *ACS Nano*, 2017, **11**, 4133–4144.
30 C.-C. Hsu, S.-L. Lin and C. A. Chang, *ACS Appl. Mater. Interfaces*, 2018, **10**, 7859–7870.
31 P. K. Pandey, A. K. Sharma, S. Rani, G. Mishra, G. Kandasamy, A. K. Patra, M. Rana, A. K. Sharma, A. K. Yadav and U. Gupta, *ACS Biomater. Sci. Eng.*, 2018, **4**, 2860–2869.
32 Y. Zhang, K. Ren, X. Zhang, Z. Chao, Y. Yang, D. Ye, Z. Dai, Y. Liu and H. Ju, *Biomaterials*, 2018, **163**, 55–66.
33 Y. Mou, M. Kang, F. Wang, M. Liu, K. Chen and R. Sun, *J. Sol-Gel Sci. Technol.*, 2017, **83**, 447–456.
34 J. Chen, X. Zhou, Y. Sheng, X. Xie, M. M. A. Abualrejal, M. Chang, Z. Shi and H. Zou, *Ceram. Int.*, 2017, **43**, 4440–4449.
35 J. Chen, Y. Sheng, Y. Song, M. Chang, X. Zhang, L. Cui, D. Meng, H. Zhu, Z. Shi and H. Zou, *ACS Sustainable Chem. Eng.*, 2018, **6**, 3533–3545.
36 C. Lin, Y. Song, F. Gao, H. Zhang, Y. Sheng, K. Zheng, Z. Shi, X. Xu and H. Zou, *J. Sol-Gel Sci. Technol.*, 2014, **69**, 536–543.

37 J. Weimmerskirch-Aubatin, M. Stoffel, A. Bouché, P. Boulet, M. Vergnat and H. Rinnert, *J. Alloys Compd.*, 2015, **622**, 358–361.
38 A.-M. Brezoiu, M. Deaconu, I. Nicu, E. Vasile, R.-A. Mitran, C. Matei and D. Berger, *Microporous Mesoporous Mater.*, 2019, **275**, 214–222.
39 C. Huo, J. Ouyang and H. Yang, *Sci. Rep.*, 2014, **4**, 3682.
40 A. G. Macedo, R. A. S. Ferreira, D. Ananias, M. S. Reis, V. S. Amaral, L. D. Carlos and J. Rocha, *Adv. Funct. Mater.*, 2010, **20**, 624–634.
41 H. Deng, F. Chen, C. Yang, M. Chen, L. Li and D. Chen, *Nanotechnology*, 2018, **29**, 415601.